Understanding the Role of Morphology in the Direct Synthesis of Diethyl Carbonate Over Ceria-Based Catalysts: An In Situ Infrared and High-Resolution TEM Study

ChemCatChem

Research Article
doi.org/10.1002/cctc.202500140

Chemistry Europe
European Chemical Societies Publishing

www.chemcatchem.org

Understanding the Role of Morphology in the Direct Synthesis of Diethyl Carbonate Over Ceria-Based Catalysts: An In Situ Infrared and High-Resolution TEM Study

Mara Arduino,[a] Enrico Sartoretti,*[a] Eleonora Calì,*[a] Samir Bensaid,[a] and Fabio Alessandro Deorsola[a]

The direct CO_2 conversion to organic carbonates such as diethyl carbonate (DEC) offers a safer alternative to conventional hazardous routes involving toxic reagents. However, the thermodynamic stability of reactants poses challenges to efficiency. In this work, nanosized ceria-based catalysts with varying morphology were synthesized through precipitation and hydrothermal method and tested to investigate the mechanism of DEC synthesis from ethanol and CO_2. In situ Fourier transform infrared (FTIR) spectroscopy revealed that CO_2 is mostly adsorbed in the form of bicarbonates and bidentate carbonates, while type I standing-up ethoxy are the most reactive ethoxy species. Additionally, signals related to the formation of monoethyl carbonate intermediate were also identified in the IR spectra collected during exposure of ethanol-saturated ceria to CO_2. High-resolution TEM analysis revealed that the rod-shaped morphology exhibits a greater abundance of surface defects, such as nanovoids and surface steps, compared to the cube and nanoparticle ones, responsible for the highest activity of the rod ceria catalyst. The rod-shaped catalyst retained high performance over four sequential regeneration and reuse cycles, demonstrating its stability and reusability. These findings provide key insights into the structure-activity relationship of ceria-based catalysts, offering a promising pathway for improving DEC synthesis from CO_2.

1. Introduction

The increasing amount of CO_2 in the atmosphere is generating global concern due to the major contribution of CO_2 emissions to the greenhouse effect. At the same time, CO_2 can be considered an inexpensive, abundant, and renewable source of carbon. Hence, much attention has been paid to the development of novel technologies for CO_2 capture and utilization[1,2] Various CO_2 utilization paths have been studied, which can be summarized into reductive and nonreductive CO_2 conversion routes.[3] The first path requires high-energy input and includes the CO_2 conversion to carbon monoxide (CO), methane, formic acid, formaldehyde, methanol, and hydrocarbons, while the second route involves the conversion to urea, carbamates, and organic carbonates.[1,2,4–12] Although only a small fraction of the total emitted CO_2 can be used this way, the sequestration of CO_2 in organic carbonates is of significant interest to the scientific community as it involves the long-term incorporation of CO_2 into useful compounds. Indeed, organic carbonates are gaining widespread attention due to their promising properties, including very low toxicity, strong solvating ability, and good biodegradability.[13] The most extensively researched linear organic carbonate is dimethyl carbonate (DMC); however, diethyl carbonate (DEC), the second homologue of the linear carbonate family is also of particular interest due to its wide range of applications.[14] It is used as an electrolyte for lithium-ion batteries and in the production of polycarbonates, an interesting and commercially successful class of polymers.[15,16] It is an excellent green solvent and can be used as a carbonylation reagent and alkylating agent instead of hazardous compounds such as phosgene or alkyl halides.[14] Due to its higher oxygen content (40.6 wt.%), DEC has also been proposed as a substitute for methyl tert-butyl ether (MTBE) as an oxygen-containing fuel additive.[17] A further advantage of DEC over MTBE, which has been identified as a common and persistent groundwater contaminant is that it is biodegradable and decomposes to CO_2 and ethanol.

Thus, efforts have been made to develop new synthetic pathways within the context of sustainable advances. For example, the alcoholysis of urea[18] and the direct conversion of alcohol and CO_2. Among them, the latter route is the most attractive from the environmental point of view thanks to the direct use of a greenhouse gas (*i.e.*, CO_2) as feedstock and the low toxicity of the reagents. Moreover, this method requires only one reaction step and produces water as the only co-product (reaction 1). Furthermore, especially for DEC synthesis, ethanol can be obtained from biomass in the biorefinery process by the fermentation of

[a] Dr. M. Arduino, Dr. E. Sartoretti, Dr. E. Calì, Prof. S. Bensaid, Prof. F. A. Deorsola
Department of Applied Science and Technology, Politecnico di Torino, Corso Duca degli Abruzzi 24, Turin 10129, Italy
E-mail: enrico.sartoretti@polito.it
eleonora.cali@polito.it

Supporting information for this article is available on the WWW under https://doi.org/10.1002/cctc.202500140

sugar, starch or lignocellulosic materials.[19] Thus, the synthesis of DEC starting from bioethanol and CO_2 is a desirable green chemistry approach.

$$2CH_3CH_2OH+CO_2 \leftrightarrows DEC+H_2O \quad (1)$$

The direct synthesis requires, however, the activation of CO_2, which is a kinetically inert and thermodynamically stable compound ($\Delta G_f^0 = -396$ kJ/mol). Hence, the exploration of catalysts with effective sites for CO_2 activation is necessary. In addition, this reaction shows thermodynamic equilibrium limitations thus, it suffers from extremely low yields[20] and is hence currently still being investigated at the laboratory scale. In detail, while the direct route to DMC has been widely researched and it is therefore considered a model route for linear carbonates synthesis.[21–23] The direct DEC synthesis from ethanol and CO_2 has been barely investigated to the best of our knowledge.[17,24–26] A wide range of homogeneous catalysts has been tested for CO_2 direct conversion, especially for DMC synthesis, such as tin alkoxides, alkali-metal halides, alkyl halides, bases, and ionic liquids.[27–29] Although they exhibit high efficiency, the major issue lies in catalyst separation and recovery. Conversely, heterogeneous catalysts are more suitable because of their superior stability and the easier separation of the catalyst from the products. To date, transition-metal oxides are the most intensively investigated heterogeneous catalysts for the direct synthesis of dialkyl carbonates.[30–35] It has been reported that CeO_2, ZrO_2, and $Ce_xZr_{1-x}O_2$ solid solutions are effective for this synthesis due to the acid-base bifunctionality of their active sites. Tomishige et al.[36] first suggested that the activity and selectivity of amphiprotic oxides for the DMC production could be related to the presence of acid and basic sites on the catalyst surface. Subsequently, numerous studies have investigated and highlighted the importance of both acid and basic sites in determining catalytic activity.[24,37–39] However, its dependence on acid-base sites has not been fully understood yet. Also, the nature of active sites could play an important role, since the presence of strong acid sites might induce alcohol dehydration and produce ether, an undesirable product.[40] Thus, further investigation is still needed to understand how the catalyst acidity and basicity should be tailored in order to obtain stable and efficient catalysts.

Several studies have been focused on unravelling the reaction mechanism of direct synthesis of DMC over ceria-based materials.[32,41,42] According to Aresta et al., CO_2 directly reacts with the methoxy group on the catalyst surface, while Santos et al.[43] proposed that CO_2 and methanol are both adsorbed on the active sites before they combine with each other to give DMC, suggesting that methanol is activated to methyl and methoxy species on acid and basic sites, respectively. Methoxy species on the basic sites then react with CO_2 to create monodentate methoxy carbonate (MMC). Finally, MMC reacts with methyl species produced on the acid sites to give DMC. It has also been suggested that the activation of methanol to methyl species on the acid sites of the catalyst is the step determining the reaction rate among these processes.[44] Therefore, a large number of acid sites could be favorable to the direct synthesis of DMC from methanol and carbon dioxide. Although it is often assumed that the mechanism of formation of DEC is similar to that of DMC and some studies have explored the mechanism of DEC synthesis through various routes (i.e., urea ethanolysis[45,46] and oxidative carbonylation[47–49]) or the ethanol activation and conversion to other valuable products,[50–52] only a few have specifically investigated ethanol activation for the direct synthesis of DEC and the identification of its reaction intermediates.[17,53]

To date, research on DEC synthesis remains limited. In particular, to the best of our knowledge, no IR study has yet been reported on the investigation of the behavior of ceria-based catalysts for the direct synthesis of DEC. Given that the direct route is both promising and challenging, this work aims to advance understanding in this field by identifying the most active species involved in the reaction and determining the key structural properties of the catalyst that promote their formation and reactivity. In the past years, the role of CeO_2 morphology on catalytic activity has been investigated. Wang et al. found that, when compared to CeO_2 nanocubes exposing the (100) facet and CeO_2 nanooctahedra exposing the (111) facet, CeO_2 nanorods with predominant (110) facet showed the highest catalytic activity for the direct production of DMC.[54] According to theoretical calculations, this was due to the adsorption of CO_2 on oxygen vacancy active sites being energetically favored; moreover the (110) surface plane of CeO_2 was found more suitable for the production of oxygen vacancies compared to the (100) and (111) facets.[55] According to in situ infrared spectroscopy characterizations, this activity improvement is caused by an active bidentate carbonate intermediate from CO_2 adsorption on surface oxygen vacancy sites of CeO_2 nanorods.[56]

As mentioned above, this reaction has very low yields. In order to increase the DEC yield, the DEC synthesis can be carried out in the presence of high CO_2 pressure or supercritical CO_2. Such conditions, however, require a high energy input for pressurization. Anyway, other alternative strategies were proposed to enhance the yield. Nonreactive dehydration systems, such as inorganic absorbents (zeolites, molecular sieves, magnesium oxide), gas phase systems, or membrane separation, have been investigated in order to remove the water product and thus beneficially affect the thermodynamics of the process.[57] These have the advantage of not interfering with the activity of the catalyst and the kinetics of the reaction, but do not satisfactorily increase the yields. Besides, reactive dehydration systems are inorganic or organic compounds that actively react with water.[57] Several reactive compounds have been tested for this purpose, such as butylene oxide, orthoesters,[58] acetals, trimethyl phosphate (TMP), ionic liquids, iodomethane (CH_3I), dicyclohexylcarbodiimide (DCC) and nitriles.[59] Among them, nitriles (acetonitrile, benzonitrile, 2-cyanopyridine) have proved to be very effective, especially when coupled with cerium-based catalysts. Honda et al. successfully achieved 94% DMC yield with 96% selectivity when using 2-cyanopyridine as the dehydration agent and CeO_2 as the catalyst. Furthermore, 2-picolinamide, obtained by hydration of 2-CP, was dehydrated using Na_2O/SiO_2 as catalyst, yielding 84% and exhibiting a selectivity higher than 99%.[31]

In the present work, CeO_2 and $Ce_xZr_{1-x}O_2$ catalysts with different morphologies and various Ce/Zr ratios were synthesized

and tested, coupled with 2-cyanopyridine (2-CP) as dehydrating agent, for the direct synthesis of DEC from ethanol and CO_2, in order to develop a process which can operate at mild conditions of moderate temperature and pressure. The DEC synthesis mechanism was originally investigated by performing in situ FTIR measurements, analyzing the catalyst interaction with carbon dioxide, ethanol and diethyl carbonate to identify active species. To further investigate the potential influence of morphology on the obtained results, high-resolution TEM analysis was also carried out.

2. Experimental Section

CeO_2 and $Ce_xZr_{1-x}O_2$ catalysts with different morphologies were prepared by the precipitation and hydrothermal methods and characterized by various techniques, such as N_2-physisorption, X-ray diffraction (XRD), field emission scanning electron microscopy (FE-SEM), transmission electron microscopy (TEM), and temperature programmed desorption analyses (CO_2-TPD and NH_3-TPD).

2.1. Catalysts Synthesis

Catalysts were prepared by using sodium hydroxide (NaOH, 98%) (Merck, Germany) as precipitating agent, cerium nitrate hexahydrate ($Ce(NO_3)_2{\bullet}6H_2O$, 99%) (Merck, Germany) as cerium ion source, and zirconium oxynitrate hydrate ($ZrO(NO_3)_2{\bullet}H_2O$, 99%) (Merck, Germany) as zirconium ion precursor.

For the synthesis of nanorods (R), 20 mL of a 1 M solution of $Ce(NO_3)_2{\bullet}6H_2O$, and $ZrO(NO_3)_2{\bullet}H_2O$ was prepared, dosing the two nitrates in the proper molar ratio. 130 mL of 6 M NaOH solution was added dropwise into the nitrates one to induce precipitation. The system was stirred at room temperature for 1 h. The suspension was then transferred into an autoclave reactor and heated up to 100 °C for 24 h. After cooling down the reactor to room temperature, the precipitate was subjected to centrifugation and washing cycles, initially with water until reaching neutral pH and subsequently with a final ethanol washing.

For the synthesis of nanocubes (C), 10 mL of a 2 M $Ce(NO_3)_2{\bullet}6H_2O$ solution, and 70 mL of an 8 M NaOH solution were prepared. The same precipitation step described before was carried out after which the suspension was transferred into an autoclave reactor and heated to 180 °C for 24 h. After cooling down the reactor to room temperature, the precipitate was centrifuged and washed as described for the nanorods.

The hydrothermal synthesis parameters were optimized based on the findings of Piumetti et al.[60] by varying the NaOH molarity and reaction temperature. This approach aimed at obtaining samples with a uniform and well-defined morphology.

Nanoparticles (NP) were also synthesized by precipitation, using 10 mL of a 4 M $Ce(NO_3)_2{\bullet}6H_2O$ solution and 70 mL of a 2 M NaOH solution. The NaOH solution was added dropwise into the nitrate one until precipitation occurred. The system was stirred for 1 h. Finally, the precipitate was centrifuged and washed as described above.

All the samples were then dried overnight at 70 °C and subsequently calcined in a muffle furnace at 550 °C with a 5 °C/min ramp for 2 h. In order to obtain a rod-shaped catalyst with a surface area similar to the cube-shaped one, a sample of rod-shaped cerium oxide (CeO_2-R) underwent an additional calcination step in a muffle furnace at 950 °C with a 5 °C/min ramp for 6 h (CeO_2-R-C950).

2.2. Catalysts Characterization

N_2 physisorption was performed by using a Micromeritics ASAP TRISTAR 3020 instrument. All samples were pretreated at 200 °C for 2 h prior to the measurements. The surface area was measured with the Brunauer–Emmett–Teller (BET) method, while the Barrett–Joyner–Halenda (BJH) desorption analysis was used to determine the pore area and specific pore volume.

The structural properties of the catalysts were investigated by X-ray diffraction (XRD) with a Panalytical X'pert diffractometer using Cu kα radiation. The diffractograms were collected in the range $20° \leq 2\theta \leq 80°$ with a scan rate of 2.0 °/min.

Surface acid and basic properties of the catalysts were determined through temperature-programmed desorption (TPD) using respectively ammonia (NH_3-TPD) and carbon dioxide (CO_2-TPD) as probe molecules. CO_2-TPD were carried out with a Thermo Scientific TPD/R/O 1100 instrument. Approximately 100 mg of powder was degassed with 30 mL/min of helium (He) at 200 °C for 2 h, the sample was then cooled to 100 °C and treated with 30 mL/min of CO_2 for 30 min. Subsequently, the physisorbed CO_2 was removed by flowing 30 mL/min of He for 30 min. Finally, the temperature was increased from 100 to 900 °C with a ramp rate of 10 °C/min and dwelled at 900 °C for 30 min.

NH_3-TPD were carried out in a quartz tube reactor placed in a PID-controlled vertical oven connected to an Infrared ABB Uras 26 analyzer module for NH_3 quantification. Approximately 300 mg of powder was inserted in the reactor and degassed with 200 mL/min of N_2 at 250 °C for 30 min, then the sample was cooled to 100 °C and treated with 200 mL/min of 2500 ppm NH_3 in a helium stream at 100 °C for 30 min. Subsequently, the physisorbed NH_3 was removed by flowing 200 mL/min of N_2 for 60 min. Finally, the TPD was carried out by flowing 200 mL/min of N_2, while the temperature was increased from 100 to 450 °C at a ramp rate of 5 °C/min and kept at 450 °C for 30 min.

Field-emission scanning electron microscopy (FE-SEM) was performed in a Zeiss Merlin operating in imaging mode at a voltage of 3 kV and equipped with a Gemini II column and an Oxford EDX detector for elemental analysis (performed at 15 kV). Transmission electron microscopy (TEM) analysis was carried out with a Thermo Scientific Talos F200X TEM, operating at a voltage of 200 kV and equipped with a CMOS 16 Mpx camera. The samples for TEM analysis were prepared by dispersion of the powder catalysts in high-purity propan-2-ol (99.8%) (Merck, Germany) followed by sonication for 10 min and then drop-cast on holey-C coated Cu TEM grids (Agar Scientific, United Kingdom) previously plasma-cleaned in Ar for 20 s.

2.3. Experimental Testing Setup

Tests were carried out in a laboratory-scale stirred autoclave reactor with an inner volume of 310 mL. Prior to the experiment, the catalyst was dried at 100 °C overnight in a drying oven. The optimum catalyst amount (1 g) was identified based on yield and productivity data obtained through preliminary screening of 0.1-2 g catalyst loadings. 2-CP was employed as a dehydrating agent, standardly used to shift the thermodynamic equilibrium towards the products.[61,62] Known amounts of ethanol, catalyst, and 2-CP were loaded in the reactor, which was then purged with CO_2 three times at room temperature. The reaction system was then pressurized up to 25 bar with CO_2. After a stabilization time, required for the CO_2 dissolution in ethanol, the reactor was heated to 130 °C and mechanically stirred (500 rpm) for 4 h. Finally, the reactor was cooled to room temperature and depressurized. The catalyst was then recovered by filtration and the reaction mixture was analyzed on an Agilent 7890A

GC-MS equipped with a HP5 MS capillary column (0.25 mm × 30 m × 0.25 μm) and quantified on an 8890 GC-FID equipped with a CP-sil 8 CB capillary column (0.32 mm × 25 m × 5 μm).

The following equations were applied to determine conversion, selectivity, and yield, where n_{in} and n_{fin} are respectively the initial and final mols of a given compound present in the reactor, while EP and EC stand for ethyl picolinate and ethyl carbamate, respectively, which are the main reaction byproducts.

$$\text{Yield (\%)} : Y = \frac{2 \times n_{\text{fin,DEC}}}{n_{\text{in,EtOH}}} \times 100$$

$$\text{Selectivity (\%)} : S = \frac{n_{\text{fin,DEC}}}{n_{\text{fin,DEC}} + n_{\text{fin,EP}} + n_{\text{fin,EC}}} \times 100$$

Recycle tests were carried out for the most active catalyst. After every run, the catalyst was thoroughly washed with ethanol and distilled water, which were then removed by drying the catalyst overnight at 70 °C.

2.4. In Situ FTIR Investigation

FTIR measurements were performed with a Bruker Invenio S spectrometer equipped with a mercury cadmium telluride detector and a quartz cell with transparent KBr windows. In situ FTIR spectra were collected in transmission mode while introducing increasing quantities of probe molecules in the IR cell containing the catalyst, previously pressed into a thin disk. Prior to the measurements, catalysts were pretreated in vacuum at 300 °C, reaching this temperature with a 5 °C/min heating rate and maintaining it for 30 min. All the spectra were subtracted with respect to the spectrum of the as-synthesized catalysts, collected at 25 °C after the pretreatment and before sending the probe molecule to the cell. CO_2, ethanol, and DEC were used as probe molecules. FTIR spectra were recorded at increasing pressures of probe molecules. Then, in order to identify the most active species, an FTIR study of ethanol adsorption followed by CO_2 adsorption was performed: after sending ethanol to the sample, physisorbed ethanol was removed by evacuation and then an increasing amount of CO_2 was sent into the IR cell. The collected IR spectra were then normalized with respect to the density of the catalyst disks.

3. Results and Discussion

3.1. Structural and Morphological Properties of the Catalysts

Figure 1a reports a comparison of the XRD patterns acquired on the synthesized catalysts. All samples exhibited the fluorite cubic structure, typical for cerium oxide, and its derivatives[63] with signals characteristic of the CeO_2 pattern (JCPDF00-004-0593). Examining the Ce-Zr-O catalysts, no peaks related to the presence of monoclinic and tetragonal zirconium oxide phases were detected, possibly suggesting that Zr was successfully doped into the ceria lattice structure. SEM-EDX measurements confirmed the desired doping ratios for all the samples with only slight deviations (± 0.015) from the aimed elemental ratios for all targeted Ce-Zr-O compositions (Table S1 and Figures S1–S4 in the Supporting Information). Nanoparticles and rod-shaped catalysts showed broader XRD peaks due to the lower crystallite size, whereas sharp peaks for cubes suggested larger particle dimensions, which was confirmed by TEM and SEM (Figures 1b,c, S5,S6, and Table S2).

The SEM and TEM analyses also revealed that the nanoparticles presented uniform particle sizes, whereas rods and cubes had greater inhomogeneity (Figures S5,S6). For the Zr-doped CeO_2 samples, despite the decrease in rod size with increasing Zr content, the rod morphology remains preserved throughout the Zr-doping amounts (Figures 1c and S7).

As reported in Table 1, the textural properties of the catalysts were affected by the synthesis method. Nanorod catalysts exhibited the highest surface area and pore volume, while nanocubes showed the lowest surface area and a rather low pore volume (physisorption isotherms of the samples are reported in Figures S8–S15). Besides, doping with zirconium resulted in a decrease in the surface area, which is in line with literature data.[42] The calcination of the rod-like catalyst (CeO_2-R) at 950 °C demonstrated remarkable efficacy in reducing its surface area to levels comparable to those of the CeO_2-C catalyst.

3.2. Acid-Base Properties of the Catalysts

As the presence of acidic and basic sites has been reported to influence catalyst activity towards the conversion from CO_2 to DEC[24,39] the synthesized samples were then tested by CO_2- and NH_3-TPD. All samples showed an intense CO_2 desorption peak between 50 and 200 °C (Figure S16a), related to weak basic sites,[38] except the CeO_2-C catalyst, as well as a small amount of medium-strong basic sites (peaks from 250 to 500 °C).[38] The total basicity calculated for each catalyst is reported in Table 1 and shows that the basicity decreased in the following order: rod-shaped > nanoparticles > cube-shaped. The CeO_2-R sample showed the highest specific number of basic sites (411 μmol/g) while, by increasing the Zr content, the basicity progressively decreased.

The acidic nature of the samples was investigated by NH_3-TPD (Figure S16b). Interestingly, the acidic behavior was affected both by the catalyst morphology and by the zirconium content. Almost no acidic sites were detected in the CeO_2-C sample, possibly due to its low surface area. CeO_2-NP showed a bimodal distribution related to the presence of weak and medium-strength acidic sites, while CeO_2-R showed the highest number of acidic sites among the undoped ceria catalysts. The increase in Zr loading was effective in enhancing the catalyst acidity while decreasing the basicity, and the $Ce_{0.80}Zr_{0.20}O_2$-R sample exhibited the highest specific number of acidic sites (107 μmol/g) as reported in Table 1.

3.3. Catalytic Activity Tests

Catalytic tests of the synthesized samples were carried out at 130 °C and 25 bar CO_2 pressure for 4 h and the catalytic activity of all samples is compared in Table 1. High values of selectivity were obtained with all the catalysts, among which the CeO_2-NP catalyst displayed the lowest one (96%). The main byproduct

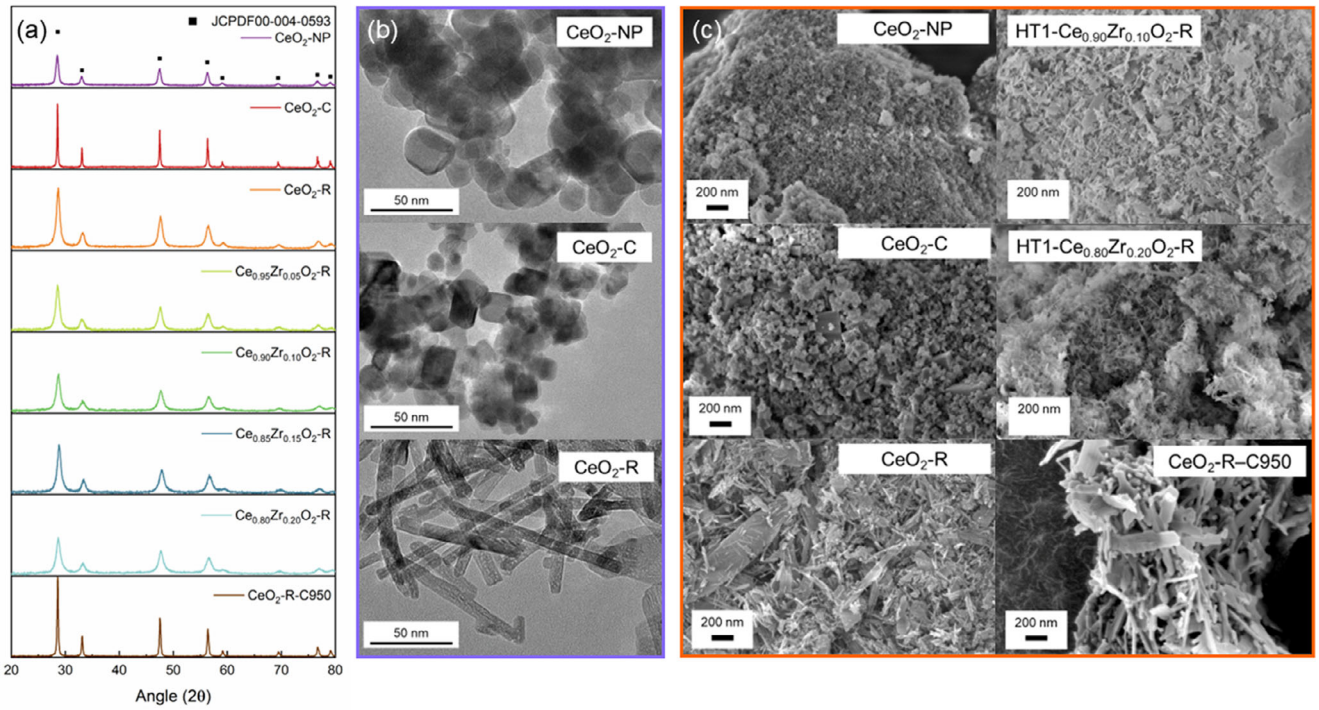

Figure 1. (a) XRD patterns of the different-morphology CeO_2 and Zr-doped CeO_2 samples described in this work: NP (nanoparticles), C (nanocubes), and R (nanorods); (b) TEM images of NP, R, and C ceria samples showing the different shapes obtained; (c) SEM characterization of the morphological distribution of these samples.

Table 1. BET surface area (BET-SA), pore properties, acidic and basic properties, and catalytic activity of the catalysts described in this work.

Catalyst	BET-SA (m^2/g)	Pore Volume (cm^3/g)	BJH Pore Size (nm)	Acidic Sites (μmol/g)	Basic Sites (μmol/g)	Yield (%)	Selectivity (%)
CeO_2-NP	53 ± 1	0.08 ± 0.02	5 ± 1	13	172	20 ± 3	96
CeO_2-C	15 ± 8	0.13 ± 0.06	28 ± 3	1	114	6 ± 2	100
CeO_2-R	98 ± 1	0.77 ± 0.12	31 ± 4	17	411	41 ± 1	98
$Ce_{0.95}Zr_{0.05}O_2$-R	97 ± 1	0.69 ± 0.01	31 ± 2	30	313	32 ± 3	98
$Ce_{0.90}Zr_{0.10}O_2$-R	95 ± 2	0.68 ± 0.01	29 ± 1	19	300	38 ± 1	99
$Ce_{0.85}Zr_{0.15}O_2$-R	87 ± 4	0.39 ± 0.04	24 ± 2	41	253	25 ± 3	99
$Ce_{0.80}Zr_{0.20}O_2$-R	96 ± 2	0.75 ± 0.03	30 ± 0	107	213	32 ± 0	98
CeO_2-R-C950	23 ± 1	0.10 ± 0.02	22 ± 0	8	250	29 ± 2	97

Reaction conditions: Ethanol quantity: 860 mmol, 2-CP quantity: 430 mmol, catalyst quantity: 1g, pressure of CO_2 at 25 °C: 25 bar, temperature: 130 °C, time: 4 h, stirring velocity: 500 rpm.

was ethyl picolinate, which can be produced upon reaction of ethanol with 2-picolinamide. The rod-shaped catalysts showed the best performance with yields varying from 25 to 40%, while the CeO_2-NP and CeO_2-C exhibited the lowest activities with yields of 20% and 6%, respectively. For the sake of comparison, catalytic tests in absence of 2-CP were also conducted to ascertain that the catalytic activity trends obtained would be analogous despite the much lower yields (Table S4).These results are in line with those obtained by different authors studying DMC synthesis.[56,64]

As frequently reported in the literature, a large number of acid and basic sites is necessary to increase the reaction yield,[65–67] provided that these are not excessively strong.[68] However, despite the increase in the acidity given by the Zr doping (Table 1), no remarkable enhancement in the catalytic activity was observed and the rod-shaped pure ceria (CeO_2-R) sample exhibited the best performances. Liu et al.[66] observed a different behavior and attributed the higher activity of the $Zr_{0.1}Ce$ sample to a greater presence of oxygen vacancies. While our study also explored this correlation (see Figures S17–S24 and Table S3), we did not find conclusive evidence to confirm it.

Even the highest number of acid sites of the $Ce_{0.80}Zr_{0.20}O_2$-R sample does not seem to have an appreciable effect on the yield (see Table 1). This sample was also tested for possible Zr leaching after 4 h and 8 h catalytic tests, with results showing a slight decrease in Zr content, from 0.24 to 0.7 after the

longest catalytic test (Table S5 and Figure S25). Instead, a correlation can be found between basicity and yield, indicating that weak- and moderate-strength basic sites promote the activity (Figure S26). Gao et al.[69] reported similar observations in their experiments, which showed that activity is linearly dependent on the number of basic sites rather than strictly linearly dependent on the acidity or the ratio between acidity and basicity.

To verify whether the obtained catalytic results were only dictated by the higher surface areas of the rod-shaped samples, a proof-of-concept experiment was performed by calcining the best-performing CeO_2-R sample to 950 °C, which resulted in a significantly decreased surface area (Table 1). When tested for the conversion of CO_2 and ethanol to DEC, this sample exhibited a substantially higher yield compared to the cube-shaped cerium oxide (29.2 versus 6.2%, respectively), despite the similar surface areas measured (23 versus 15 m^2/g) as reported in Table 1.

Many works suggest that the catalytic reactivity of CeO_2 can be also attributed to the presence of oxygen vacancies or to the Ce^{3+}/Ce^{4+} ratio.[35,70–73] Even if their role in the current reaction cannot be totally ignored, Ce^{3+} cations are unlikely to be involved because this reaction occurs under mild and nonreducing conditions. On the other hand, oxygen vacancies could act as basic sites capable of adsorbing CO_2 as carbonates. Therefore, mainly acid and basic sites are expected to catalyze this reaction. The similar results obtained when testing the $Ce_{0.85}Zr_{0.15}O_2$-R and the CeO_2-R-C950 samples (which have the same number of basic sites) corroborate this hypothesis, as a very similar yield was obtained for these samples (25.3% versus 29.2%, respectively), despite the remarkably lower surface area measured for the rod-shaped sample calcined at 950 °C (23.0 m^2/g versus 87.2 m^2/g for $Ce_{0.85}Zr_{0.15}O_2$-R). Nonetheless, these results suggest that the morphology seems to affect the number of basic sites obtained, and, as a consequence, the catalytic activity: indeed, all rod-shaped samples reported a higher number of basic sites compared to the spherical and cube-shaped samples (Table 1), in line with previous findings by Wang at al.[64]

Table 2 compares the results of this study with previously reported catalytic performance for the direct synthesis of DEC, expressed as catalyst productivity ($mmol_{DEC}/g_{cat.}$). The use of dehydrating agents significantly enhanced productivity compared to reactions conducted without them. Moreover, reactive dehydrating agents such as 2-cyanopyridine, butylene oxide, and triethyl orthoacetate proved to be more effective than nonreactive alternatives like molecular sieves, which led to productivity values that were two orders of magnitude lower.[22,39,74] Giram et al. also observed higher activity for the CeO_2 catalyst compared to the Ce-Zr mixed oxide. While a direct comparison is difficult due to differences in reaction parameters, the CeO_2-R sample shows a productivity that is relatively close to that reported by Giram et al., despite their reaction being carried out at twice the pressure. This suggests that CeO_2-R may have favorable properties under the conditions used in this study.

3.4. Mechanistic Investigation Through In Situ FTIR

In situ FTIR analyses were performed to investigate whether morphology played a role in the reaction mechanism. For this FTIR investigation, the CeO_2-R and CeO_2-C samples were selected, as they showed the highest and lowest activity, respectively.

First, the two catalysts were exposed to increasing pressures of the probe molecules, that is CO_2, ethanol, and DEC; detailed results about the species forming on the samples are reported in the Supporting Information (Figures S27–S32, Tables S6 and S7). Briefly, CO_2 mostly adsorbs forming bicarbonates and bidentate carbonates on both materials; monodentate and polydentate carbonates appear too, but in minor proportion. Ethanol adsorption on the two CeO_2 samples gives rise to three types of ethoxy species: (i) monodentate ethoxy, also known as standing up or type I, (ii) bidentate ethoxy, also known as lying down or type II, and (iii) tridentate ethoxy, also known as type III. Monodentate species, which are more labile, are prevalent on CeO_2-R, while type II and type III ethoxy, more stable, preferentially form on CeO_2-C.

Then, in order to identify the most active species and elucidate the possible differences in the reaction mechanism for the two analyzed catalysts, an in situ FTIR study of ethanol adsorption followed by CO_2 adsorption was performed. When the two ceria catalysts with pre-adsorbed ethanol were exposed to CO_2, the FTIR spectra changed considerably. From Figure 2a, it can be observed that bands at 1121, 1063, and 905 cm^{-1}, attributable to type I ethoxy species,[50,52] significantly decreased, whereas the intensity of bands at 1103, 1053, 888, and 882 cm^{-1} showed only a slight decrease. The CeO_2-C catalyst also showed the same trend as illustrated in Figure 2b. This suggests that type I ethoxy could be more reactive than other ethoxy species in the cases presented here. In the frequency range 1800–1200 cm^{-1}, the bands at 1575, 1475, 1402, 1381, 1318, and 1300 cm^{-1} were found to increase. Despite the bands at 1575, 1402, and 1300 may also be related to the adsorption of CO_2 with formation of bidentate carbonates and bicarbonate species (see Table S6), the bands at 1381 and 1318 cm^{-1} are only present in the DEC adsorption spectra as highlighted in Figure 2e and Figure 2f; hence, these bands could be related to the formation of the diethyl carbonate or be ascribed to the monoethyl carbonate as a reaction intermediate. It is suggested, however, that the production of the intermediate is more favorable and that DEC is not detected given the low-pressure analytical conditions.[66,76] Various studies on the reaction mechanism of DMC indicate that observing features of DMC is challenging under typical experimental conditions due to its low concentration. Nevertheless, according to the principle of microreversibility, the decomposition of a compound should follow the same elementary steps that led to its synthesis.[77] Consequently, the dissociation of DEC on the surface may reveal the intermediate needed to produce DEC. The suggestion arises from observations during the adsorption of diethyl carbonate on the catalysts (See Figures S31 and S32), which revealed specific wavenumber signals associated with the presence of ethoxy and carbonates. This suggests that diethyl carbonate undergoes initial dissociation into ethoxy and monoethyl carbonate,

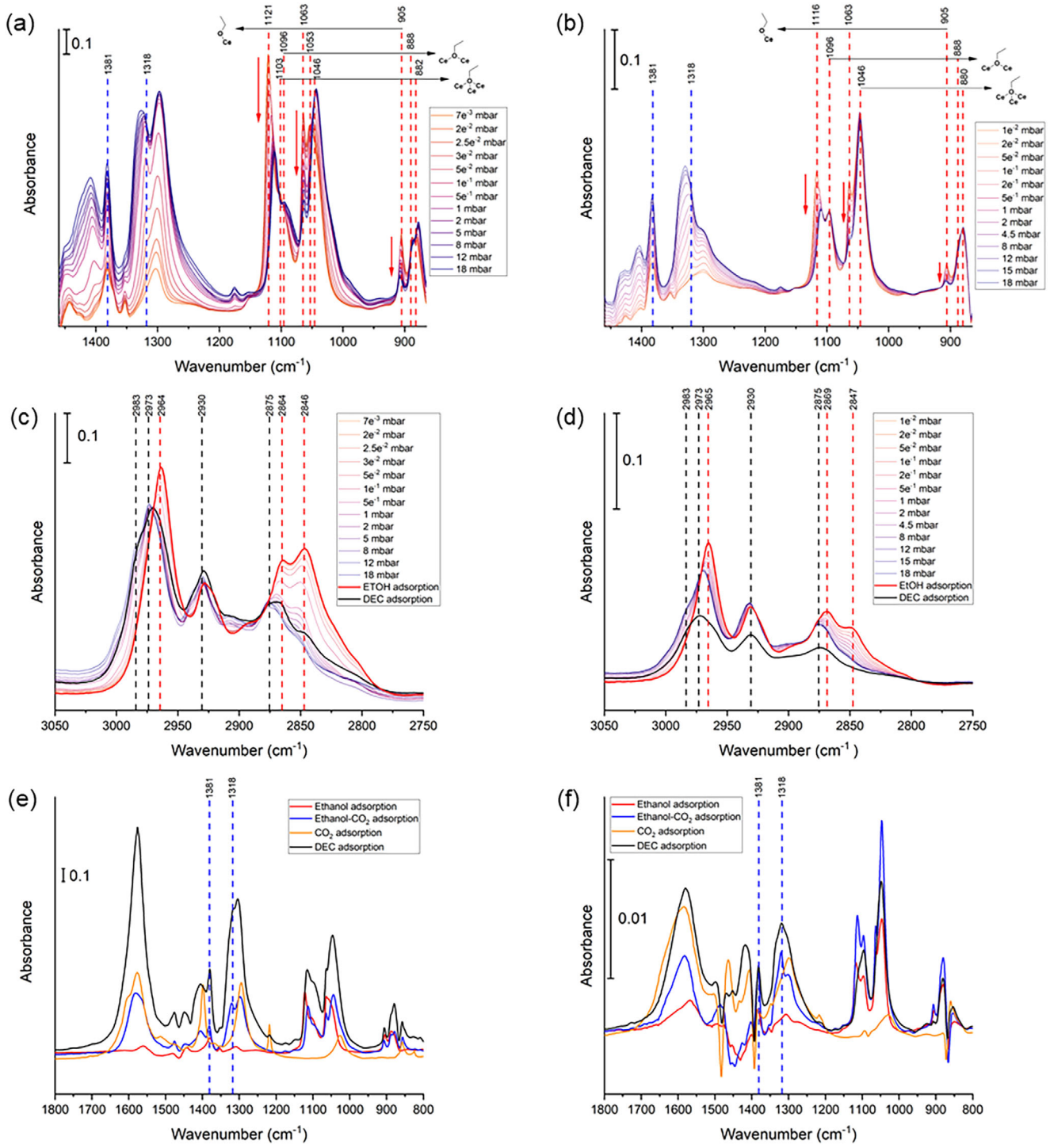

Figure 2. FTIR spectra of CO_2 adsorption on pre-adsorbed ethanol in the frequency range 1460–860 cm^{-1} on (a) the CeO_2-R catalyst and (b) the CeO_2-C catalyst (red dashed lines correspond to signals associated with ethanol adsorption, while blue dashed lines indicate the signals arising from CO_2 + ethanol reaction, leading to the formation of DEC or monoethyl carbonate intermediate); FTIR spectra of CO_2 adsorption on pre-adsorbed ethanol in the frequency range 3050–2750 cm^{-1} on the (c) CeO_2-R catalyst and (d) the CeO_2-C catalyst (black dashed lines refer to CH_x stretching IR frequencies of adsorbed DEC, while red dashed lines correspond to CH_x stretches of adsorbed ethanol); comparison between the IR spectra of all the in situ experiments carried out for (e) CeO_2-R catalyst and (f) CeO_2-C catalyst, with each spectrum corresponding to the highest pressure of probe molecule sent to the catalysts for ethanol, CO_2, DEC, and ethanol + CO_2.

Table 2. Catalytic performance of different catalysts in the direct synthesis of DEC, as reported in previous studies and the current work.

Catalyst	Synthesis Conditions	Test Conditions	Productivity ($mmol_{DEC}/g_{cat.}$)	REF
CeO_2-R	Direct NaOH precipitation and hydrothermal treatment at 100 °C for 24 h. Calcination at 550 °C for 2 h	EtOH: 860 mmol, 2-CP: 430 mmol, catalyst: 1 g, P: 25 bar, T: 130 °C, t: 4 h	178	This work
CeO_2	Direct ammonia precipitation at 50 °C and pH 10. Calcination at 600 °C for 4 h	EtOH: 337 mmol, catalyst: 0.2 g, P: 40 bar, T: 120 °C, t: 4 h	3.20	[75]
CeO_2	Supplied by Daiichi Kigenso Kagaku Kogyo, CeO_2-HS. Calcination at 600 °C for 3 h	EtOH: 140 mmol, catalyst: 0.5 g, P: 65 bar (120 °C), T: 120 °C, t: 4 h	0.314	[58]
CeO_2	Supplied by Daiichi Kigenso Kagaku Kogyo, CeO_2-HS. Calcination at 600 °C for 3 h	EtOH: 140 mmol, 2,2-Diethoxypropane: 21 mmol, catalyst: 0.5 g, P: 65 bar (120 °C),T: 120 °C, t: 4 h	1.6	[58]
CeO_2	Supplied by Daiichi Kigenso Kagaku Kogyo, CeO_2-HS. Calcination at 600 °C for 3 h	EtOH: 100 mmol, 2-CP: 50 mmol, catalyst: 0.1 g, P: 50 bar, T: 150 °C, t: 3 h	225.2	[39]
$Ce_{0.9}Zr_{0.1}O_{2-\delta}$	Urea precipitation followed by hydrothermal synthesis at 120 °C for 8 h. Calcination at 600 °C for 5 h	EtOH: 100 mmol, 2-CP: 50 mmol, catalyst: 0.1 g, P: 50 bar,T:150 °C, t: 3 h	46.5	[39]
CeO_2	Reverse NH_4OH precipitation at pH 11. Calcination at 600 °C for 3 h	EtOH: 314 mmol, butylene oxide: 19 mmol, catalyst: 1 g, P: 5 bar, T: 180 °C, t: 25 h	2	[38]
CeO_2	Supplied by Daiichi Kigenso Kagaku Kogyo. No calcination	EtOH: 43 mmol, triethylorthoacetate: 11 mmol, catalyst: 0.04 g, P: 50 bar, T: 160 °C, t: 20 h	131	[74]
CeO_2	Supplied by Daiichi Kigenso Kagaku Kogyo. No calcination	EtOH: 43 mmol, triethylorthoacetate: 11 mmol, catalyst: 0.37 g, P: 50 bar, T: 160 °C, t: 120 h	24,1	[74]
ZrO_2	NH_4OH precipitation. Calcination at 600 °C for 2 h	EtOH: 343 mmol, catalyst: 0.5 g, P: 70 bar, T: 150 °C, t: 2 h	0.3	[26]
ZrO_2	NH_4OH precipitation. Calcination at 600 °C for 2 h	EtOH: 343 mmol, catalyst: 0.5 g, molecular sieve: 0.1 g, P: 70 bar, T: 150 °C, t: 2 h	0.71	[26]

followed by subsequent breakdown into carbonates and ethoxy. Based on the experiments presented here, we speculate that the unassigned frequencies (1381 and 1318 cm^{-1}) correspond to the monoethyl carbonate intermediate.

The intermediate formation could also be verified by comparing the FTIR spectra of the ethanol-CO_2 adsorption with the DEC adsorption on the rod catalyst in the range of νCH_x (3000–2800 cm^{-1}). As reported in Figure 2c, by incrementing the CO_2 pressure, a gradual peak shift from the CH_x stretching frequencies related to ethanol adsorption to the CH_x stretches associated with DEC adsorption was observed. Indeed, the FTIR spectra collected at high CO_2 loading are nearly identical to the DEC adsorption spectrum. Thus, observing the FTIR spectra in this region allowed to identify the reaction pathway for the rod catalyst.

The same investigation was carried out for the CeO_2-C catalyst (see Figure 2d): by incrementing the CO_2 amount, a peak shift from peaks related to ethanol adsorption to peaks linked to DEC adsorption was also observed in this case. However, the final spectrum retained more similarities to the ethanol adsorption spectrum than to the one of DEC, suggesting a significant presence of unreacted ethoxy species on the catalyst surface. This can be verified by analyzing the spectra of the two catalysts when performing in situ ethanol adsorption (Figures S29 and S30). Specifically, ethanol interacts with the catalyst surface by producing ethoxy species. According to several works, these bands may be generated by ethanol dissociation on the CeO_2 surface into two types of ethoxy species with different thermal stability. Monodentate ethoxy are more labile (E_{ads} = −0.95 eV), while bidentate ethoxy are more stable species (E_{ads} = −2.68 eV).[52] DFT calculations revealed that another type of ethoxy species can also be obtained when ethanol adsorbs on the hydroxylated CeO_2 surface, named type III ethoxy, which is a tridentate type.[50] From the two spectra, it can be noted that the CeO_2-C sample showed the presence of more type III ethoxy groups than type I; the former species do not react with CO_2 to produce DEC since the intensity of the associated peaks (1046 and 880 cm^{-1}) remain unchanged, as evident in Figure 2b.

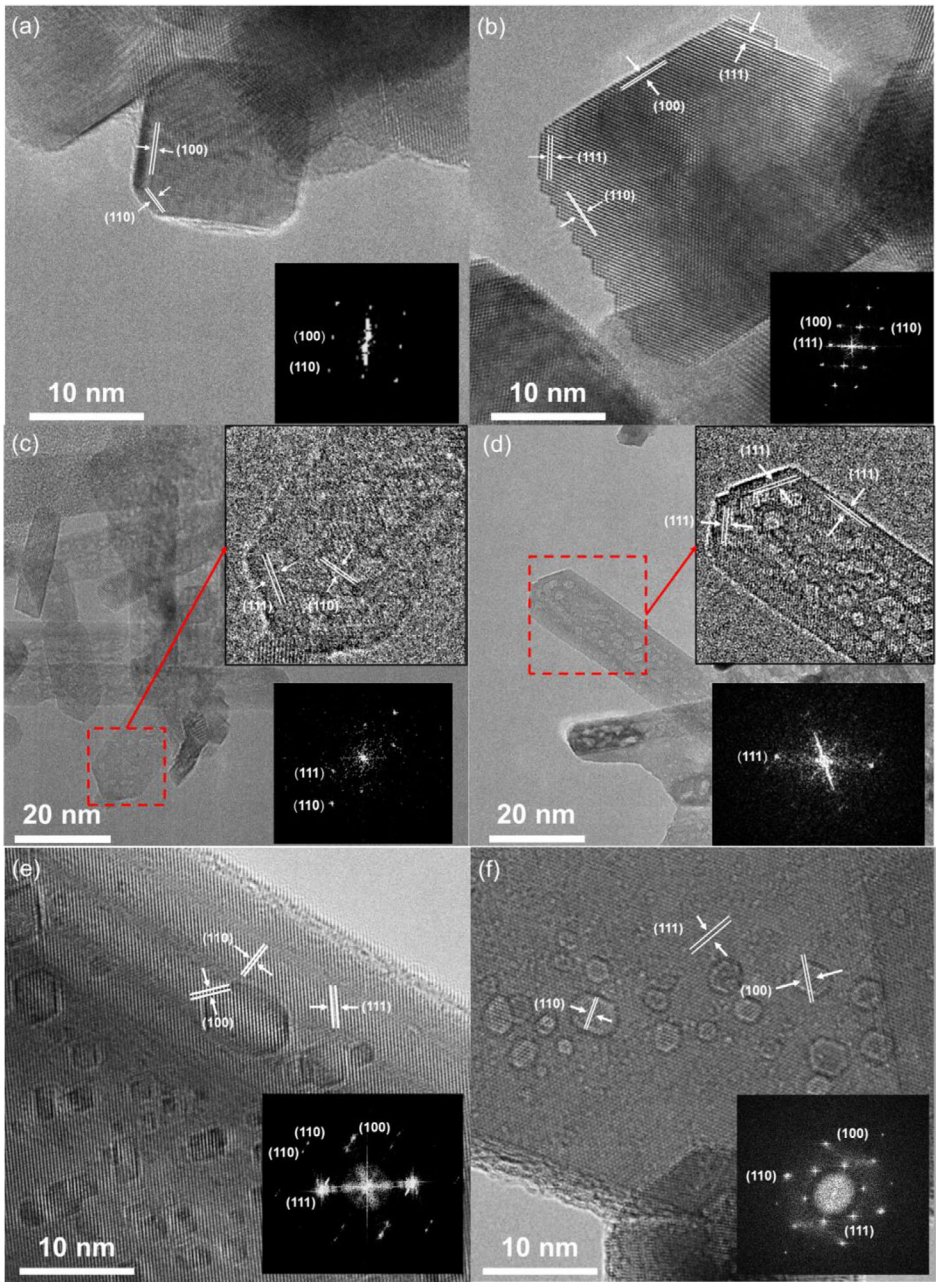

Figure 3. TEM and FFT images of (a) and (b) the CeO_2-C catalyst, showing a homogeneous-contrast surface, (c) and (d) the CeO_2-R catalyst, and (e) and (f) the CeO_2-R-C950 catalyst for which the lower-contrast defects are extensively observed throughout the analyzed areas.

3.5. Investigating the Role of Morphology Through High-Resolution Electron Microscopy and FFT Analysis

To understand the possible role of morphology in the observed catalytic results and mechanistic elucidation, the morphology of the two catalysts was further examined by TEM analysis. When imaging the rod catalyst at high resolution, several irregularities were found. These defects, which appear as areas of lower contrast as can be seen in Figure 3, are instead absent in ceria cubes and nanoparticles. Interestingly, the presence of such defects is also found quite pronounced in the CeO_2-R-C950 catalyst. Recently, it has been proposed that defect chemistry in CeO_2 can play a crucial role in boosting its activity when employed for several catalytic reactions.[78–81] Previous work has suggested that voids within ceria nanorods are developed through aggregation of oxygen vacancies within the body of the nanorod during synthesis.[82] This is in line with our work, as in the CeO_2-R-C950 sample bigger and elongated voids are observed, which are suggested by earlier research to be formed through the aggregation of adjacent voids at higher temperatures, aiming to minimize the overall surface energy.[83] This finding would therefore explain the observed higher activity of this catalyst compared to the cube-shaped CeO_2, despite the similar surface area, suggesting that such defects are responsible for the increased catalytic performance.

Fast Fourier Transform (FFT) analysis was hence carried out on the acquired images to investigate the possible correlation of void formation with specific crystal facets. The analysis showed preferentially (100) planes for the CeO_2-C catalyst, while (111) and (110) exposed facets were mainly found for the CeO_2-R catalyst. Previous research has correlated the presence of surface defects to the crystal structure and exposed facets of CeO_2-based materials, as based on the different formation energies of oxygen defects for the different crystal planes.[84,85] Specifically, it has been proposed by experimental and DFT findings that the (110) crystal plane has a lower energy of formation of oxygen vacancies compared to (100) and (111) facets, consequently resulting in a higher amount of oxygen defects, and hence increasing the reactivity and catalytic performance.

Moreover, Figure 3e and 3f show that larger pits are obtained for the sample calcined at higher temperature (950 °C); these voids exhibit symmetry with clearly defined facets, predominantly consistent with {100}-truncated {111}-octahedra. Lattice fringes cross the void region by retaining the same orientation and there is no evidence of moiré patterns, implying that these voids are enclosed inside a single crystal grain, rather than consisting of smaller grains that would exhibit a different contrast due to an out-of-focus effect. This feature hence suggests that the single crystalline structure remains continuous despite the defects. Brambila et al. studied the evolution of voids with the calcination temperature in rod- and cube-shaped cerium oxide samples, and they evaluated through DFT simulations the amount of energy needed to remove oxygen from the nanoceria surface. Their work showed that extracting surface oxygen from a nanorod with voids is thermodynamically easier compared to ceria nanorods lacking voids.[82] Furthermore, previous studies have demonstrated that the most stable step edges of nanoislands and pits on the ceria (111) surface correspond to (110) and (100) facets.[86] When tested for methanol adsorption, these were found to serve as active sites, where methanol dissociates to form methoxy on step edges resembling (110) facets and bridging methoxy on those resembling (100) facets.[86] Consequently, the simulations suggested that voids activate {111} surfaces. According to these results, as our rod catalysts expose mostly the (110) and the defective (111) crystal planes, similar findings can be drawn on the dissociation of ethanol on ceria nanorods. Thus, our results suggest that ethanol adsorbs on these facets preferentially as type I ethoxy, while on the (100) plane the bridging and three-coordinated ethoxy formation is mostly favored.[87] The highest activity of the rod-shaped cerium oxide catalysts could therefore be attributed to the presence of such mesoporous structural defects, such as clustered vacancy voids preferentially formed on certain facets.

Based on these results, a possible reaction mechanism is proposed for the DEC synthesis with the CeO_2-R catalyst, as illustrated in Figure 4. According to this, type I ethoxy species adsorbed on the catalyst surface defects react with adsorbed bidentate carbonate or bicarbonate species to give rise to monoethyl carbonates. Finally, their interaction with another ethoxy species produces DEC and water. A comparable mechanism has been proposed for the CeO_2-C catalyst in Figure 5: the key differences are the dissociation of ethanol into type III ethoxy for this catalyst, and the limited adsorption of CO_2 on the (100) plane, which result in reduced formation of intermediates and, consequently, lower diethyl carbonate production.

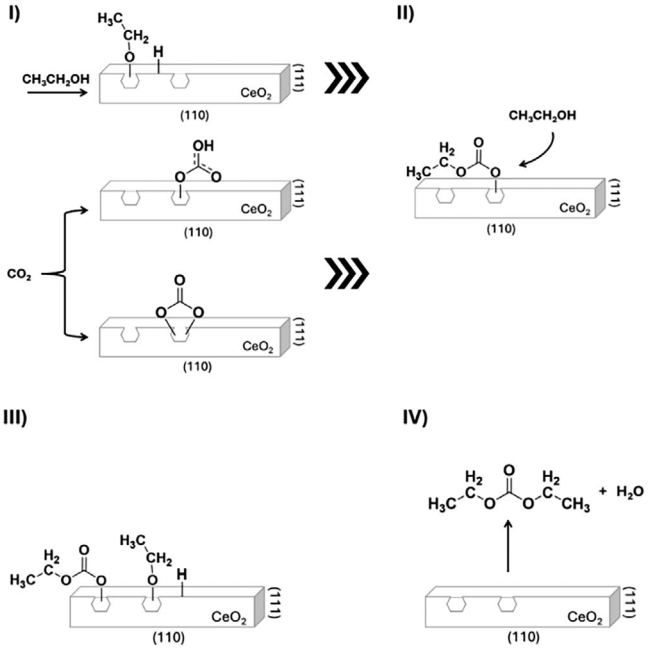

Figure 4. Scheme of the proposed reaction mechanism on the CeO_2-R catalyst.

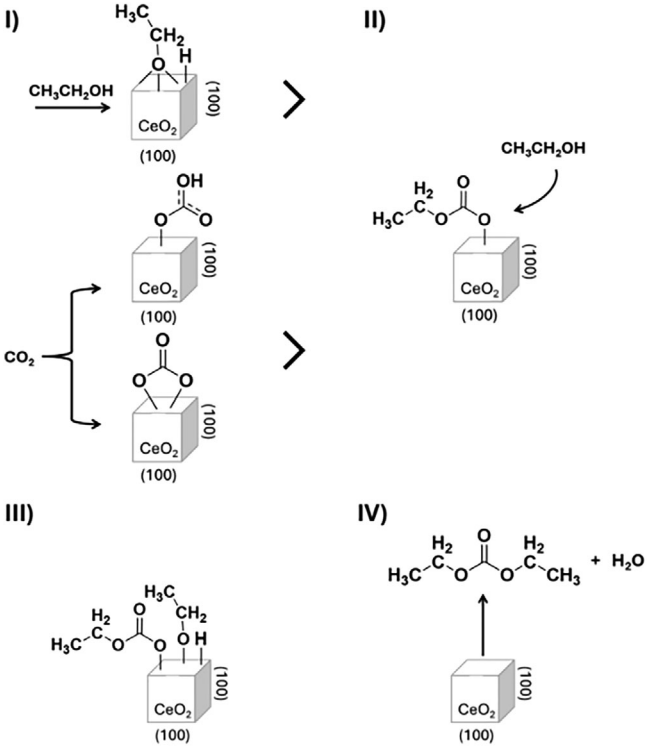

Figure 5. Scheme of the proposed reaction mechanism on the CeO_2-C catalyst.

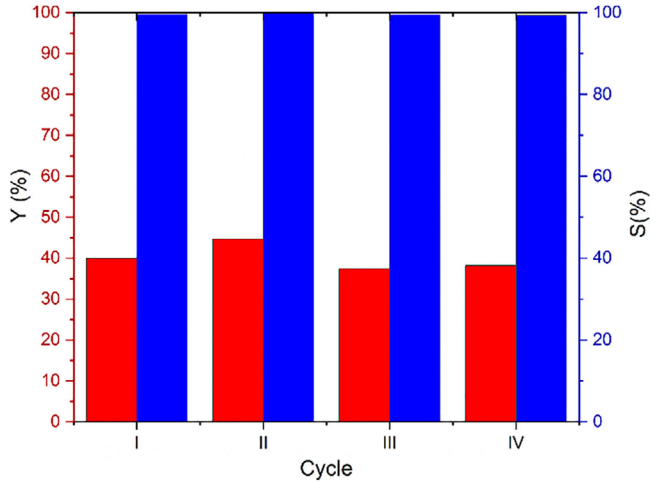

Figure 6. Recycle tests for the CeO_2-R catalyst. (Ethanol quantity: 0.86 mol, 2-CP quantity: 0.43 mol, catalyst quantity: 1 g, P_{CO2} at 25 °C: 25 bar, temperature: 130 °C, time: 4 h, stirring velocity: 500 rpm.)

3.6. Catalyst Stability Investigation

Finally, to verify the possible reuse of the best-performing catalyst presented in this work, recycling tests were carried out at the same operating conditions for the CeO_2-R catalyst, which showed the highest catalytic activity. As shown in Figure 6, the catalytic performance was retained for four sequential cycles with only a very slight decrease in selectivity (from 99.6% for cycle I to 99.4% after the IV cycle). These results highlight the catalyst excellent stability, as it maintains its activity and selectivity over several uses, requiring less frequent replacement and demonstrating promising feasibility and sustainability in a real application scenario.

4. Conclusion

In this work, cerium-based catalysts with different morphologies were synthesized through the precipitation and the hydrothermal synthesis methods and then tested for the DEC direct synthesis from ethanol and CO_2. The synthesis method affects the properties of the catalysts, and morphology was found to play a key role in the catalytic activity towards DEC direct synthesis. Rod ceria-based catalysts displayed the highest catalytic activity followed by nanoparticles and cubic-shaped ceria. Despite doping with Zr was effective in increasing the acidic character of the catalyst, Ce-Zr mixed oxides showed a lower activity with respect to the pure ceria rod catalyst; the latter sample was characterized by a higher number of basic sites, suggesting that acidity plays a secondary role in comparison to basicity.

To understand the mechanism behind the catalytic activity, in situ FTIR investigation was performed on the CeO_2-R and CeO_2-C catalysts, exhibiting respectively the highest and the lowest catalytic activity. The results showed that type I ethoxy is more reactive than the other ethoxy species, as the FTIR signals of type I ethoxy quickly disappeared when increasing the CO_2 pressure, indicating its conversion. The main difference between the two catalysts was found in the mechanism of ethanol activation, with the formation of type I and II ethoxy species for CeO_2 rods, whereas of type II and III ethoxy species for cube-shaped CeO_2. To address the lack of understanding on DEC adsorption on CeO_2 surfaces, this was also investigated, as studying the FTIR spectra in the νCH_x region can be useful to understand if the DEC production has occurred. Our new results indeed allowed us to identify and understand the different reaction pathways for the rod- and cube-shaped catalysts. Finally, high-resolution TEM and FFT analyses were performed to investigate the reason behind these differences. We found that extensive structural defects were present in the rod-shaped catalysts, which were instead absent in the cube-shaped ceria. By combining the acidity-basicity, mechanistic, and structural investigation results, we were able to understand the observed superior catalytic activity exhibited by the best-performing rod-shaped sample, which was demonstrated to be active and stable even after four consecutive catalytic tests. Overall, these results elucidate the advantages of tuning the morphology and defect chemistry of CeO_2-based catalysts for their most efficient use in the DEC direct synthesis from ethanol and CO_2.

Supporting Information

A file including additional SEM and TEM images, nitrogen adsorption-desorption isotherms, XPS, CO_2-TPD, and NH_3-TPD profiles, and in situ CO_2, ethanol, and DEC adsorption FTIR spectra is available in the Supporting Information. The authors have cited additional references within the Supporting Information file.[88–93]

Acknowledgements

The authors acknowledge the funding received by the Italian Ministero dell'Università e della Ricerca (MUR) under the Dipartimento di Eccellenza 2018–2022 program and the PON Ricerca e Innovazione "REACT-EU" project (DM 1062/21).

Open access publishing facilitated by Politecnico di Torino, as part of the Wiley - CRUI-CARE agreement.

Conflict of Interests

The authors declare no conflict of interest.

Data Availability Statement

The data that support the findings of this study are available from the corresponding author upon reasonable request.

Keywords: Ceria nanostructures · CO_2 capture and utilization · Defect chemistry · Diethyl carbonate · Sustainable chemistry

[1] M. Aresta, F. Nocito, A. Dibenedetto, in *Advances in Catalysis*, (Ed: C. Song), Elsevier, Amsterdam, the Netherlands **2018**, Vol. *62*, Ch. 2.
[2] M. Aresta, A. Dibenedetto, A. Angelini, *Chem. Rev.* **2014**, *114*, 1709–1742.
[3] R. G. Grim, Z. Huang, M. T. Guarnieri, J. R. Ferrell, L. Tao, J. A. Schaidle, *Energy Environ. Sci.* **2020**, *13*, 472–494.
[4] I. Omae, *Coord. Chem. Rev.* **2012**, *256*, 1384–1405.
[5] K. Tomishige, M. Tamura, Y. Nakagawa, *Chem. Rec.* **2019**, *19*, 1354–1379.
[6] A. Rizzetto, M. Piumetti, R. Pirone, E. Sartoretti, S. Bensaid, *Catal. Today* **2024**, *429*, 114478.
[7] A. Rizzetto, E. Sartoretti, M. Piumetti, R. Pirone, S. Bensaid, *Chem. Eng. J.* **2024**, *501*, 157585.
[8] F. M. Baena-Moreno, M. Rodríguez-Galán, F. Vega, B. Alonso-Fariñas, L. F. Vilches Arenas, B. Navarrete, *Energy Sources, Part A Recover. Util. Environ. Eff.* **2019**, *41*, 1403–1433.
[9] F. Salomone, E. Sartoretti, S. Ballauri, M. Castellino, C. Novara, F. Giorgis, R. Pirone, S. Bensaid, *Catal. Today* **2023**, *423*, 114023.
[10] A. J. Kamphuis, F. Picchioni, P. P. Pescarmona, *Green Chem.* **2019**, *21*, 406–448.
[11] M. Signorile, D. Salusso, V. Crocellà, M. C. Paganini, S. Bordiga, F. Bonino, D. Ferri, *Phys. Chem. Chem. Phys.* **2023**, *25*, 8392–8402.
[12] W. S. Putro, A. Ikeda, S. Shigeyasu, S. Hamura, S. Matsumoto, V. Y. Lee, J. C. Choi, N. Fukaya, *ChemSusChem* **2021**, *14*, 842–846.
[13] T. Tabanelli, D. Bonincontro, S. Albonetti, F. Cavani, in *Studies in Surface Science and Catalysis: Horizons in Sustainable Industrial Chemistry and Catalysis*, (Eds: S. Albonetti, S. Perathoner, E. A. Quadrelli), Elsevier, Amsterdam, the Netherlands, Vol *178*, **2019**, Ch 7.
[14] O. Kreye, L. C. Over, T. Nitsche, R. Z. Lange, M. A. R. Meier, *Tetrahedron* **2015**, *71*, 293–300.
[15] R. Zhou, J. Liu, L. Jia, X. Lü, Z. Song, *Inorg. Chem. Commun.* **2018**, *90*, 57–60.
[16] S. Matsumura, S. Harai, K. Toshima, *Macromol. Chem. Phys.* **2000**, *201*, 1632–1639.
[17] K. Shukla, V. C. Srivastava, *RSC Adv.* **2016**, *6*, 32624–32645.
[18] K. Shukla, V. C. Srivastava, *Fuel Process. Technol.* **2017**, *161*, 116–124.
[19] L. Mojović, D. Pejin, O. Grujić, S. Markov, J. Pejin, M. Rakin, M. Vukašinović, S. Nikolić, D. Savić, *Chem. Ind. Chem. Eng. Q.* **2009**, *15*, 211–226.
[20] M. F. O'Neill, M. Sankar, U. Hintermair, *ACS Sustainable Chem. Eng.* **2022**, *10*, 5243–5257.
[21] S. Huang, B. Yan, S. Wang, X. Ma, *Chem. Soc. Rev.* **2015**, *44*, 3079–3116.
[22] E. Leino, P. Mäki-Arvela, V. Eta, N. Kumar, F. Demoisson, A. Samikannu, A. R. Leino, A. Shchukarev, D. Y. Murzin, J. P. Mikkola, *Catal. Today* **2013**, *210*, 47–54.
[23] M. Honda, S. Kuno, N. Begum, K. I. Fujimoto, K. Suzuki, Y. Nakagawa, K. Tomishige, *Appl. Catal. A Gen.* **2010**, *384*, 165–170.
[24] O. Arbeláez, A. Orrego, F. Bustamante, A. L. Villa, *Catal. Letters* **2016**, *146*, 725–733.
[25] E. Leino, P. Mäki-Arvela, V. Eta, D. Y. Murzin, T. Salmi, J. P. Mikkola, *Appl. Catal. A Gen.* **2010**, *383*, 1–13.
[26] X. Zhang, D. Jia, J. Zhang, Y. Sun, *Catal. Letters* **2014**, *144*, 2144–2150.
[27] J. Du, J. Shi, Z. Li, Z. Liu, X. Fan, C. Tao, *J. Nat. Gas Chem.* **2012**, *21*, 476–479.
[28] J. Sun, S. I. Fujita, M. Arai, *J. Organomet. Chem.* **2005**, *690*, 3490–3497.
[29] A. H. Tamboli, A. A. Chaugule, H. Kim, *Fuel* **2016**, *166*, 495–501.
[30] M. Honda, M. Tamura, Y. Nakagawa, K. Nakao, K. Suzuki, K. Tomishige, *J. Catal.* **2014**, *318*, 95–107.
[31] M. Honda, M. Tamura, Y. Nakagawa, S. Sonehara, K. Suzuki, K. I. Fujimoto, K. Tomishige, *ChemSusChem* **2013**, *6*, 1341–1344.
[32] A. H. Tamboli, N. Suzuki, C. Terashima, S. Gosavi, H. Kim, A. Fujishima, *Catalysts* **2021**, *11*, 223.
[33] C. Daniel, Y. Schuurman, D. Farrusseng, *J. Catal.* **2021**, *394*, 486–494.
[34] M. Zhang, *Sci. J. Chem.* **2019**, *7*, 105.
[35] S. Xu, Y. Cao, Z. Liu, *Catal. Commun.* **2022**, *162*, 106397.
[36] K. Tomishige, T. Sakaihori, Y. Ikeda, K. Fujimoto, **1999**, *58*, 225–229.
[37] I. Prymak, V. N. Kalevaru, S. Wohlrab, A. Martin, *Catal. Sci. Technol.* **2015**, *5*, 2322–2331.
[38] E. Leino, N. Kumar, P. Mäki-Arvela, A. Aho, K. Kordás, A. R. Leino, A. Shchukarev, D. Y. Murzin, J. P. Mikkola, *Mater. Chem. Phys.* **2013**, *143*, 65–75.
[39] G. G. Giram, V. V. Bokade, S. Darbha, *New J. Chem.* **2018**, *42*, 17546–17552.
[40] D. T. Sarve, S. K. Singh, J. D. Ekhe, *Inorg. Chem. Commun.* **2022**, *139*, 109397.
[41] C. M. Marin, L. Li, A. Bhalkikar, J. E. Doyle, X. C. Zeng, C. L. Cheung, *J. Catal.* **2016**, *340*, 295–301.
[42] A. H. Tamboli, A. A. Chaugule, S. W. Gosavi, H. Kim, *Fuel* **2018**, *216*, 245–254.
[43] B. A. V. Santos, C. S. M. Pereira, V. M. T. M. Silva, J. M. Loureiro, A. E. Rodrigues, *Applied Catal. A, Gen.* **2013**, *455*, 219–226.
[44] K. Tomishige, Y. Ikeda, T. Sakaihori, K. Fujimoto, *J. Catal.* **2000**, *192*, 355–362.
[45] S. Xin, L. Wang, H. Li, K. Huang, F. Li, *Fuel Process. Technol.* **2014**, *126*, 453–459.
[46] D. Wang, B. Yang, X. Zhai, L. Zhou, *Fuel Process. Technol.* **2007**, *88*, 807–812.
[47] N. S. Roh, B. C. Dunn, E. M. Eyring, R. J. Pugmire, H. L. C. Meuzelaar, *Fuel Process. Technol.* **2003**, *83*, 27–38.
[48] A. Punnoose, M. S. Seehra, B. C. Dunn, E. M. Eyring, *Energy and Fuels* **2002**, *16*, 182–188.
[49] H. Wang, Y. Xiang, M. Guo, J. Su, G. Wang, W. Cui, Z. Deng, *Energy and Fuels* **2020**, *34*, 8697–8706.
[50] J. Podobiński, M. Zimowska, M. Śliwa, J. Datka, *Molecules* **2023**, *28*, 1251.
[51] J. Vecchietti, P. Lustemberg, E. L. Fornero, M. Calatayud, S. E. Collins, S. Mohr, M. V. Ganduglia-Pirovano, J. Libuda, A. L. Bonivardi, *Appl. Catal. B Environ.* **2020**, *277*, 119103.
[52] J. Vecchietti, P. Pérez-Bailac, P. G. Lustemberg, E. L. Fornero, L. Pascual, M. V. Bosco, A. Martínez-Arias, M. V. Ganduglia-Pirovano, A. L. Bonivardi, *ACS Catal.* **2022**, *12*, 10482–10498.
[53] F. Gasc, S. Thiebaud-Roux, Z. Mouloungui, *J. Supercrit. Fluids* **2009**, *50*, 46–53.
[54] Z. Fu, Y. Zhong, Y. Yu, L. Long, M. Xiao, D. Han, S. Wang, Y. Meng, *ACS Omega* **2018**, *3*, 198–207.
[55] A. A. Marciniak, F. J. F. S. Henrique, A. F. F. de Lima, O. C. Alves, C. R. Moreira, L. G. Appel, C. J. A. Mota, *Mol. Catal.* **2020**, *493*, 111053.
[56] S. Y. Zhao, S. P. Wang, Y. J. Zhao, X. B. Ma, *Chinese Chem. Lett.* **2017**, *28*, 65–69.
[57] M. Honda, M. Tamura, Y. Nakagawa, K. Tomishige, *Catal. Sci. Technol.* **2014**, *4*, 2830–2845.
[58] T. Chang, M. Tamura, Y. Nakagawa, N. Fukaya, J. C. Choi, T. Mishima, S. Matsumoto, S. Hamura, K. Tomishige, *Green Chem.* **2020**, *22*, 7321–7327.
[59] P. Kumar, V. C. Srivastava, U. L. Štangar, B. Mušič, I. M. Mishra, Y. Meng, *Catal. Rev. – Sci. Eng.* **2021**, *63*, 363–421.
[60] M. Piumetti, S. Bensaid, T. Andana, M. Dosa, C. Novara, F. Giorgis, N. Russo, D. Fino, *Catalysts* **2017**, *7*, 174.
[61] L. Tian, Y. S. Liao, Z. Xiao, G. Sun, J. P. Chou, C. Y. Wong, J. C. Ho, Y. Zhao, P. T. Chou, Y. K. Peng, *ACS Catal.* **2024**, *14*, 16861–16871.
[62] W. Sun, P. Li, M. Yabushita, Y. Nakagawa, Y. Wang, A. Nakayama, K. Tomishige, *ChemSusChem* **2023**, *16*, e202300768.
[63] S. Ballauri, E. Sartoretti, M. Castellino, M. Armandi, M. Piumetti, D. Fino, N. Russo, S. Bensaid, *ChemCatChem* **2024**, *16*, e202301359.
[64] S. Wang, L. Zhao, W. Wang, Y. Zhao, G. Zhang, X. Ma, J. Gong, *Nanoscale* **2013**, *5*, 5582.
[65] H. J. Lee, W. Joe, I. K. Song, *Korean J. Chem. Eng.* **2012**, *29*, 317–322.
[66] B. Liu, C. Li, G. Zhang, X. Yao, S. S. C. C. Chuang, Z. Li, *ACS Catal.* **2018**, *8*, 10446–10456.
[67] K. H. Kang, W. Joe, C. H. Lee, M. Kim, D. B. Kim, B. Jang, I. K. Song, *J. Nanosci. Nanotechnol.* **2013**, *13*, 8116–8120.
[68] W. Wang, S. Wang, X. Ma, J. Gong, *Catal. Today* **2009**, *148*, 323–328.
[69] J. Gao, J. Yang, T. Ma, J. Wang, D. Xia, J. Gao, J. Yang, T. Ma, J. Wang, D. Xia, B. Du, Y. Cui, C. Yang, *Chinese Chem. Lett.* **2023**, 108395.
[70] K. Tomishige, Y. Gu, T. Chang, M. Tamura, Y. Nakagawa, *Mater. Today Sustain.* **2020**, *9*, 100035.
[71] I. Prymak, V. N. Kalevaru, P. Kollmorgen, S. Wohlrab, A. Martin, *DGMK Tagungsbericht* **2013**, *2013*, 249–256.
[72] Z. Fu, Y. Yu, Z. Li, D. Han, S. Wang, M. Xiao, Y. Meng, *Catalysts* **2018**, *8*, 164.
[73] W. F. Kuan, W. Y. Yu, F. Y. Tu, C. H. Chung, Y. C. Chang, M. M. Lin, T. H. Yu, L. J. Chen, *Chem. Eng. J.* **2022**, *430*, 132941.
[74] W. S. Putro, Y. Munakata, S. Ijima, S. Shigeyasu, S. Hamura, S. Matsumoto, T. Mishima, K. Tomishige, J. C. Choi, N. Fukaya, *J. CO_2 Util.* **2022**, *55*, 101818.
[75] M. Buchmann, M. Lucas, M. Rose, *Catal. Sci. Technol.* **2021**, *11*, 1940–1948.

[76] K. T. Jung, A. T. Bell, **2001**, *347*, 339–347.
[77] L. Chen, S. Wang, J. Zhou, Y. Shen, Y. Zhao, X. Ma, *RSC Adv.* **2014**, *4*, 30968–30975.
[78] C. Yang, Y. Lu, L. Zhang, Z. Kong, T. Yang, L. Tao, Y. Zou, S. Wang, *Small Struct.* **2021**, *12*, 202100058.
[79] G. Pampararo, E. Sartoretti, A. S. Traoré, O. Ersen, C. Novara, S. Bensaid, D. P. Debecker, *J. Environ. Chem. Eng.* **2025**, *13*, 116753.
[80] M. Dosa, M. J. Marin-figueredo, E. Sartoretti, C. Novara, F. Giorgis, S. Bensaid, D. Fino, N. Russo, M. Piumetti, *Catalysts* **2022**, *12*, 364.
[81] S. Rojas-Buzo, D. Salusso, A. Jouve, E. Bracciotti, M. Signorile, S. Bordiga, *Appl. Catal. B Environ. Energy* **2024**, *346*, 123723.
[82] C. Brambila, D. C. Sayle, M. Molinari, J. Nutter, J. M. Flitcroft, T. X. T. Sayle, T. Sakthivel, S. Seal, G. Möbus, *J. Phys. Chem. C* **2021**, *125*, 10077–10089.
[83] C. Brambila, J. Nutter, M. Molinari, D. C. Sayle, T. Sakthivel, S. Seal, G. Möbus, *J. Nanoparticle Res.* **2022**, *24*, 227.
[84] Y. Cao, L. Zhao, T. Gutmann, Y. Xu, L. Dong, G. Buntkowsky, F. Gao, *J. Phys. Chem. C* **2018**, *122*, 20402–20409.
[85] A. Trovarelli, J. Llorca, *ACS Catal.* **2017**, *7*, 4716–4735.
[86] C. Yang, F. Bebensee, A. Nefedov, C. Wöll, T. Kropp, L. Komissarov, C. Penschke, R. Moerer, J. Paier, J. Sauer, *J. Catal.* **2016**, *336*, 116–125.
[87] F. Polo-Garzon, Z. Bao, X. Zhang, W. Huang, Z. Wu, *ACS Catal.* **2019**, *9*, 5692–5707.
[88] S. Ballauri, E. Sartoretti, C. Novara, F. Giorgis, M. Piumetti, D. Fino, N. Russo, S. Bensaid, *Catal. Today* **2022**, *390–391*, 185–197.
[89] A. Pinna, E. Cali, G. Kerherve, G. Galleri, M. Maggini, P. Innocenzi, L. Malfatti, *Nanoscale Adv.* **2020**, *2*, 2387–2396.
[90] C. Cocuzza, E. Sartoretti, C. Novara, F. Giorgis, S. Bensaid, N. Russo, D. Fino, M. Piumetti, *Catal. Today* **2023**, *423*, 114292.
[91] H. Idriss, *Surf. Sci.* **2021**, *712*, 121894.
[92] J. Zhang, S. Zhao, Y. Zhao, X. Ma, S. Wang, *Asia-Pacific J. Chem. Eng.* **2021**, *16*, 1–8.
[93] D. Salusso, G. Grillo, M. Manzoli, M. Signorile, S. Zafeiratos, M. Barreau, A. Damin, V. Crocellà, G. Cravotto, S. Bordiga, *ACS Appl. Mater. Interfaces* **2023**, *15*, 15396–15408.

Manuscript received: January 24, 2025
Revised manuscript received: May 7, 2025
Accepted manuscript online: May 17, 2025
Version of record online: May 31, 2025